Journal of the Optical Society of America B

OPTICAL PHYSICS

Multimodal interference model for bound states in the continuum and unidirectional guided resonances

Thomas Delplace[1,*] and **Bjorn Maes**[1,2]

[1] Micro- and Nanophotonic Materials Group, Research Institute for Materials Science and Engineering, University of Mons, Place du Parc, 20, 7000 Mons, Belgium

[2] Bjorn.Maes@umons.ac.be

*Thomas.Delplace@umons.ac.be

Received 23 October 2024; revised 11 February 2025; accepted 11 February 2025; posted 14 February 2025; published 20 March 2025

Many recent applications of photonic resonant modes have focused on optical bound states in the continuum (BICs) within photonic crystal slabs. An asymmetric kind of lossy resonances, called unidirectional guided resonances (UGRs), with intentional symmetry breaking leading to directional leakage, has also attracted considerable attention. This study presents a microscopic semi-analytical model aimed at enhancing the understanding of these resonances. We employ a multimodal interference method for BIC and UGR investigation in two-dimensional (2D) and three-dimensional (3D) structures, offering valuable insights into their specific properties. Through this model, we seek to advance the design and comprehension of both BICs and UGRs in photonic crystal slabs. To illustrate this, we examine different families of modes in a 2D device, and we explain the origin of resonances in an experimentally studied 3D structure. In both cases, symmetry breaking and judicious Bloch mode mixing form the basis of the confinement scenarios.

https://doi.org/10.1364/JOSAB.546001

1. INTRODUCTION

Resonances in photonic crystals (PhCs) attract significant interest due to their diverse applications, including lasers, optical filters, and sensors, among others [1,2]. In particular, modes called bound states in the continuum (BICs) [3–6] are notable for their exceptionally high-quality (Q-)factors and remarkable robustness against perturbations [7], offering many application opportunities in the fields of sensing, lasers, strong coupling, and nonlinear optics [8–21]. Recently, a new type of resonance, the unidirectional guided resonance (UGR), was identified [22,23]. These resonances share similar properties with BICs, but they permit radiation emission in a single direction at a specific frequency, thus opening up a range of practical applications, spanning from on-chip lasers to energy-efficient grating couplers [24–26]. Consequently, it is crucial to accurately describe and elucidate the emergence of these guided or semi-guided modes.

Several models are employed to characterize BICs, such as topological charges [7,22,27] and the decomposition into localized multipoles [28,29]. Another approach involves a multimodal decomposition of resonances [30–32], which describes BICs as the result of destructive interference between several Bloch modes guided transversely in the PhC. However, this method is usually applied to relatively simple, symmetrical structures and typically involves the interaction of only two or three modes in 2D structures.

In this paper, we introduce a semi-analytical model based on this multimodal approach, generalized to any number of Bloch modes, enabling the study of asymmetric structures, and thus the description of UGRs via the multimodal framework. We will demonstrate that this model is effective in both 2D and 3D contexts. An additional advantage of our approach is its computational efficiency, allowing rapid screening for a broad range of parameters, thereby facilitating the search for BICs or UGRs within the parameter space. We will apply this model to various structures, including a 1D periodic PhC composed of 2D rectangular particles with broken top-down symmetry, resulting in a simple staircase configuration that supports the emergence of UGRs. We show that two families of UGRs arise, with two different mode-mixing origins: one from an accidental BIC (also called Friedrich–Wintgen BIC) and the other from a symmetry-protected BIC. Furthermore, the method will be tested on a 3D structure formed by a 2D PhC made of paired cylindrical particles. The latter structure has been experimentally characterized for sensing purposes, among others [33], making it valuable to understand these resonances in detail using our model.

Section 2 introduces the semi-analytical model and its implementation. Section 3 presents the findings when the method is applied to a staircase-like asymmetric structure with UGRs. Section 4 showcases the results for the 3D structure.

2. MODEL FORMULATION

To illustrate the method, we consider a PhC consisting of symmetric rectangular sections [Fig. 1(a)], which manifests BICs. The structure is periodic along the x axis with period a and invariant along the z axis. Later on, we will break the top-down symmetry to create a PhC with staircase-shaped elements [Fig. 1(c)], which supports UGRs.

We proceed by defining a sectioning line in the middle of the structure [red dashed lines in Figs. 1(a) and 1(b)]. This section defines a 1D periodic refractive index profile along x [noted as $n(x)$]. If we consider this profile infinite along y, this provides a number of propagating modes (in y direction) defined by the 1D PhC profile $n(x)$. For the full structure, the model then follows these local Bloch modes that are propagating up and down (along y), as the complete structure is finite (along y), leading to reflections at the interfaces; see arrows in Fig. 1(b).

The number of propagating modes of the multilayer or waveguide array $n(x)$ depends on the structure and frequency. For this explanation, we focus on a case with two coexisting modes (which is a common case for BICs), though the model is applicable to an arbitrary number of modes. We then compute the waveguide array dispersion to identify all the (typically propagative) Bloch modes for a given frequency and for a given lateral propagation constant k_x.

Next, we calculate the half-turn scattering–reflection matrices, S_u and S_d for the upper and lower parts, respectively, by employing the modal properties of the upper and lower parts of the structure. These matrices provide reflection information for the entire structure, incorporating both propagation and interface reflection for the two half-structures. For a rectangular half, as in the lower part of Fig. 1(b), we construct the S_d matrix as

$$S_d = P(L_d) \times R_d \times P(L_d), \tag{1}$$

where R_d is the reflection matrix at the bottom interface, and $P(L_d)$ is the propagation matrix for a length L_d [with convention $\exp(i\omega t)$]:

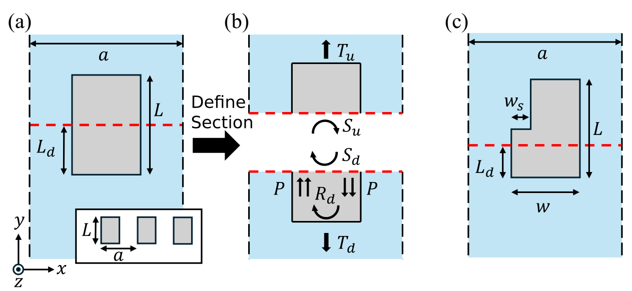

Fig. 1. (a) Unit cell of the symmetric PhC, periodic along x (periodic repetition in inset). The length L_d is rapidly adjustable analytically. (b) Detailed view of the multimodal decomposition in two halves. S_d includes the propagation of modes (described by P), which are then reflected (by R_d) and propagated again (by P). A similar reasoning applies to the upper part for S_u. (c) Staircase structure formed by the breaking of top-down symmetry.

$$P(L) = \begin{bmatrix} \exp(-i\beta_1 L_d) & 0 \\ 0 & \exp(-i\beta_2 L_d) \end{bmatrix}, \tag{2}$$

with β_1 and β_2 the (potentially complex) mode propagation constants. Once we have determined R_d, via numerical simulation, e.g., it is straightforward to calculate S_d for another length, allowing for a rapid exploration of a wide range of different lengths without computationally intensive simulations. As the resonances stem from Bloch modes bouncing up and down within the structure, being able to quickly vary the length is crucial for rapidly determining BICs and UGRs.

This decomposition is simple for the homogeneous parts of a structure, such as both parts in Fig. 1(b) and the lower part of the step structure in Fig. 1(c). However, the upper part in Fig. 1(c) has an additional interface due to the step (if one cuts as indicated with the horizontal dashed line) and therefore cannot be as easily decomposed.

The matrices S_u and S_d are central to our model. By multiplying them, we obtain the round-trip matrix $S_d S_u$ (or $S_u S_d$ if starting downward), which provides comprehensive information about a complete cycle of modes in the structure. By calculating the eigenvalues, we get

$$S_d S_u v_u = \lambda v_u, \tag{3}$$

where the eigenvalues λ provide valuable information about the localization of resonances in the parameter space. For a resonance to occur, several conditions must be met. First, $\mathrm{Im}(\lambda) = 0$ indicates a phase resonance, which is an important condition to have the same reflection criteria after each round-trip made by the modes within the structure. Second, we require constructive interference within the section, which implies having amplitudes of the same sign after a complete cycle. This condition is expressed as $\mathrm{Re}(\lambda) > 0$.

Furthermore, the eigenvectors v_u reveal the mode mixture and the relative phases between the guided modes in the particular resonance, allowing us to identify their nature. This mode mixing is often essential for achieving a good resonance, as the modes do not necessarily have a 100% reflection at the interfaces of our structure when considered individually (unless there is an orthogonality), so their interference is needed to cut (or enhance) radiation to the outside.

For BICs, the closer $|\lambda|$ is to 1, the closer we are to achieving a "true" BIC, i.e., with an infinite Q-factor, in opposition to quasi-BICs (qBICs), which have a high but finite Q-factor. Specifically, an eigenvalue of 1 signifies zero losses after a round-trip and thus corresponds to a true BIC.

However, the latter criteria are not ideal for UGRs, as these modes experience fairly significant losses in one direction (and few or no losses in the other direction), thus typically resulting in the total round-trip eigenvalue distant from 1 (so $|\lambda| < 1$). It is therefore necessary to identify another criterion that allows for distinguishing UGRs from other resonances. To do this, we calculate the transmission separately for the upper and lower parts of the particular resonance, respectively T_u and T_d [see Fig. 1(b)], which then allows us to determine the Q-factors of the two halves; see below.

Equation (3) represents the complete round-trip of the modes using the mode mixture given by the eigenvector v_u "beginning" by the upper half, thereby indicating the respective amplitudes of modes to be injected upward that achieve the resonance. In this way, we can interpret $v'_d = S_u v_u$ as the mode mixture returning from the upper part after a half round-trip S_u, containing information on propagation and reflection at the upper interface. Similarly, $v'_u = S_d S_u v_u$ can be seen as the mixture from a full round-trip in the structure. As the sum of the modulus-squared components gives us the relative power in each mode, we can calculate the amount of energy reflected by each half turn (neglecting the absorption) [34]. Thus, one can determine T_u, the transmission to the top, as one minus the reflection, which is the ratio of the reflected energy $\sum_i |v'_{d,i}|^2$ to the injected energy $\sum_i |v_{u,i}|^2$ (with i indicating the included Bloch modes). Similarly, one finds T_d, leading to

$$T_u = 1 - \frac{\sum_i |v'_{d,i}|^2}{\sum_i |v_{u,i}|^2} \qquad T_d = 1 - \frac{\sum_i |v'_{u,i}|^2}{\sum_i |v'_{d,i}|^2}. \tag{4}$$

Although this development started the cycle upward, it is possible to show that T_u and T_d can be rewritten as

$$T_u = 1 - |c_u|^2 \qquad T_d = 1 - |c_d|^2, \tag{5}$$

where

$$S_u v_u = c_u v_d \qquad S_d v_d = c_d v_u. \tag{6}$$

Here v_u and v_d are normalized eigenvectors of, respectively, $S_d S_u$ and $S_u S_d$ (i.e., $\sum_i |v_{u,i}|^2 = 1$ and $\sum_i |v_{u,i}|^2 = 1$) with the same eigenvalue λ. This reformulation allows for detachment from the arbitrary choice of the initial direction by enabling the direct calculation of T_u and T_d using the matrices S_u and S_d, along with their respective eigenvectors.

With the transmissions T_u and T_d, it is possible to determine a Q-factor associated with both the upper (Q_u) and lower (Q_d) sides of the structure, thereby enabling distinction between BICs and UGRs [34]:

$$Q_u = \frac{2\omega_0 L}{|v_g| T_u} \qquad Q_d = \frac{2\omega_0 L}{|v_g| T_d}, \tag{7}$$

where ω_0 is the angular frequency of the resonance, L is the total height [Fig. 1(a)], and v_g is an averaged group velocity computed as

$$v_g = |v_g^1||v_{u,1}|^2 + |v_g^2||v_{u,2}|^2, \tag{8}$$

with v_g^1 and v_g^2 group velocities of the considered propagating modes at the angular frequency ω_0.

Equation (7) and more precisely Eq. (8) are strictly valid for rectangular structures [Fig. 1(a)]. For the UGRs, we use a structure with a small step, resulting in a minor difference between group velocities in the upper and lower parts, allowing us to approximate and retain these equations despite the asymmetry of our structure. In cases of a more pronounced asymmetry, such as a larger step, it is necessary to detail the calculation of the Q-factor, taking into account the different regions with varying guided modes. Furthermore, we neglect evanescent modes (even though they can easily be added), as well as the energy outside the PhC. It may be possible to include a term accounting for this external field if required [35].

All the equations in this section are presented for two guided Bloch modes of the 1D periodic, lateral refractive index profile at the considered section. It should be noted that the model is easily generalizable to a general amount of N modes. The main difference is that the various matrices involved (S_u, S_d, R_u, R_d, and P) would be $N \times N$ matrices, implying N eigenvalues and N eigenvectors with N components.

3. MODEL APPLICATION TO 2D UGRs

To illustrate our model and its usefulness to elucidate new types of modes, we study a 1D PhC comprising a 2D rectangular particle. An up-down symmetric geometry [Fig. 1(a)] and a symmetry-broken, stair-shaped device [Fig. 1(c)] are considered. The symmetric structure allows obtaining (quasi-)BICs, while the asymmetric structure enables UGRs. For Fig. 1(a), up-down symmetry gives the same values for T_u and T_d, so this always leads to symmetric BIC modes. In Fig. 1(c), up-down symmetry is broken, rendering different transmissions, and in general providing modes that are unidirectional. We have chosen a step structure because it should be feasible to fabricate, and it is a perfect application of our model (e.g., for rapid length sweeps). Other types of up-down symmetry breaking are possible, e.g., with slanted sidewalls [22].

We assume a refractive index of $n = 3.5$ for the interior material and air $n = 1$ for the exterior. The cell width is $a = 386$ nm, while the particles have a width of $w = 0.6a$ and a total height of $L = 0.81a + L_d$ for the rectangle particle and $L = 1.0125a + L_d$ for the stair-like particle. The step is placed at a distance of $0.81a$ from the top of the stair. With the cut as in Figs. 1(a) and 1(c), we can semi-analytically vary the length L_d of the lower part. In contrast, varying the frequency always necessitates new calculations. To measure the asymmetry of the structure, we define an asymmetry parameter, similar to Ref. [36], $\alpha_s = w_s/w$, where w_s is the width of the step. Furthermore, we set $k_x = 0.193(2\pi/a)$ (unless otherwise stated), and for the asymmetric structure, we fix $\alpha_s = 0.08$. These values will lead to a well-defined UGR.

Figure 2(a) shows the dispersion of Bloch modes propagating in the y direction, with electric field oriented along the z axis (transverse electric, TE modes), so these are the Bloch modes as if the central section at the position of the cut was infinite vertically (and periodic along x). When the frequency increases, the number of propagating modes increases. We confine our analysis to a frequency range with two guided modes [light blue zone in the middle of Fig. 2(a)], with mode profiles in Fig. 2(b). Although it is possible to apply the multimodal method to an arbitrary number of modes, the decision to limit the study to a region containing only two modes is motivated by the desire to keep the model relatively simple and to achieve high-quality resonances. Indeed, our method relies on the principle of interference between multiple modes, and achieving good matching between the different modes is more likely with two modes than with three or more.

After computing S_u and S_d, and by applying the selection criteria on λ, namely $\mathrm{Im}(\lambda) = 0$ and $\mathrm{Re}(\lambda) > 0$, we obtain Fig. 3(a) for the symmetric structure, indicating the resonance positions in the parameter space, with color bar for the Q-factor. Two sets of quasi-parallel lines are observed: One set is more vertical and crosses the bottom dashed line [around $\omega = 0.3(2\pi c/a)$]; these are the Fabry–Pérot resonances connected with mode 1.

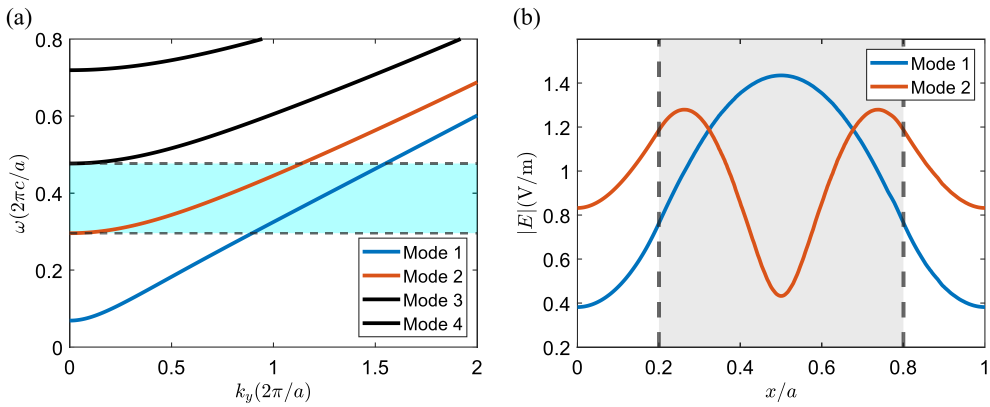

Fig. 2. (a) Dispersion of guided Bloch modes in the cut section of the PhC. We focus on the frequency range containing only two modes, highlighted by the light blue band in the middle of the graph. The blue (lowest) and orange (second lowest) lines represent the two most fundamental modes, labeled "mode 1" and "mode 2," respectively. (b) Electric field profiles of modes 1 and 2 for a wavelength of 1229 nm (or a normalized angular frequency of 0.314), shown in the same colors as in (a). The gray zone between dashed vertical lines indicates the high-index section. For both figures, $k_x = 0.193(2\pi/a)$.

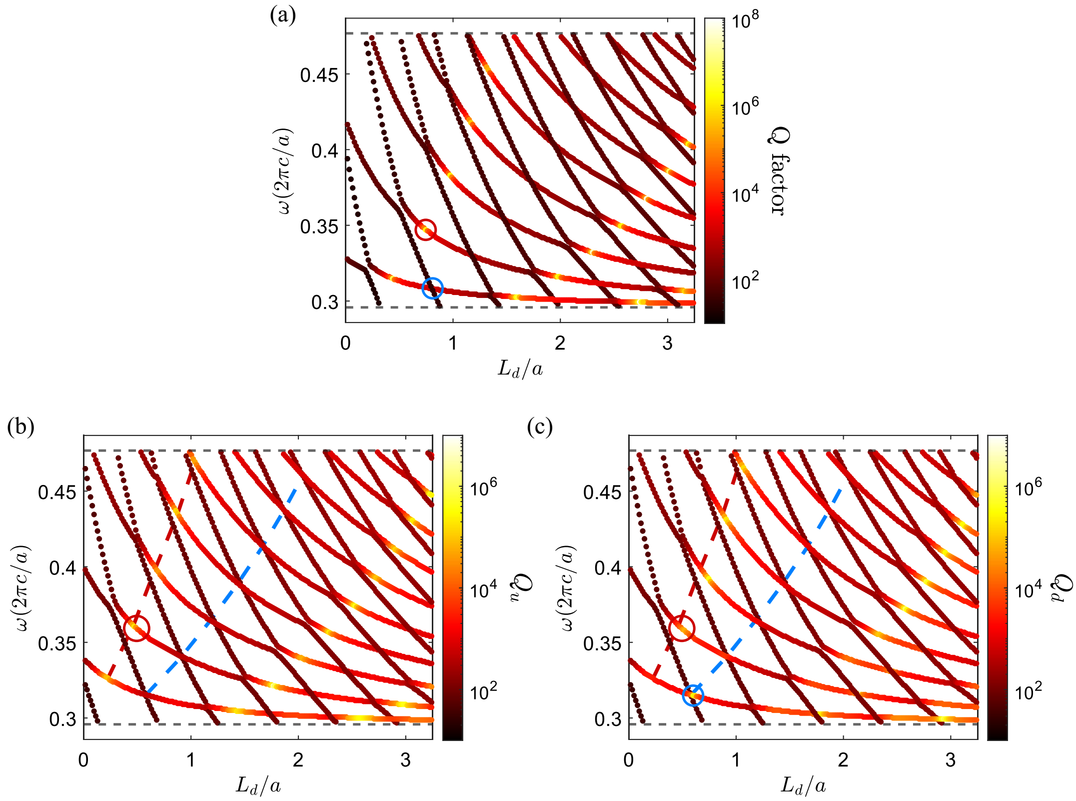

Fig. 3. In the three graphs, each point corresponds to the location of a resonance satisfying the criteria outlined in the text. (a) The color represents the global Q-factor of each point for a symmetric structure. The red circle (highest circle) highlights the qBIC associated with the "anticrossing" family. The blue circle (lowest circle) indicates the absence of a BIC at the crossing. (b), (c) Color shows top and bottom Q-factors for the asymmetric stair-like structure. The red circle (highest circle) and dashed line show the first family, referred to as "anticrossing." The blue circle and dashed line (lowest circle and line) indicate the "crossing" family.

The second set also slopes downward as the length increases but becomes nearly horizontal near the cut-off of mode 2 [around $\omega = 0.3(2\pi c/a)$, where its k_y value approaches zero]; these lines are thus the Fabry–Pérot resonances via mode 2 [31].

We calculate dispersions and reflection matrices via the finite-element solver COMSOL Multiphysics, but any tool could be employed for the model. Figure 3(a) corresponds to the symmetric structure, with three series of yellow hotspots corresponding to qBICs, which are echoes of true symmetry-protected BICs obtained only with a zero k_x. These points, see, e.g., the red circle, are located near the anticrossings between the two families of curves, indicating an interaction

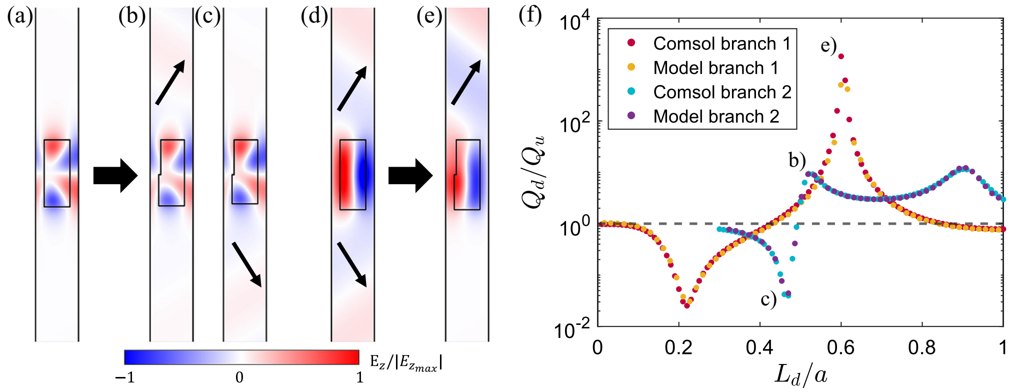

Fig. 4. (a)–(e) Out-of-plane electric field profiles for different resonances. (a) $\omega = 0.347(2\pi c/a)$, $L_d/a = 0.745$; (b) $\omega = 0.358(2\pi c/a)$, $L_d/a = 0.518$; and (c) $\omega = 0.361(2\pi c/a)$, $L_d/a = 0.470$ show the first family: (a) for the BIC, (b) and (c) for the UGRs. (d) $\omega = 0.308(2\pi c/a)$, $L_d/a = 0.810$ and (e) $\omega = 0.315(2\pi c/a)$, $L_d/a = 0.599$ show the second family: (d) for the BIC and (e) for the UGR. Black arrows show the direction of radiation propagation. (f) Comparison of the ratio between Q_d and Q_u obtained using an eigensolver (COMSOL) and the multimodal method.

between the two modes that produce this qBIC. Next to the anticrossings, there are also crossings (see, e.g., the blue circle) with dark color, indicating the absence of a (good-quality) qBIC for this up-down symmetric structure, as the up-down parities of the single-mode Fabry–Pérot resonances do not match and thus have no overlap (maximum versus zero in the middle).

Figures 3(b) and 3(c) show Q_u and Q_d for the step asymmetric structure. Large values (yellow zones) are observed at (sometimes slightly) different positions, indicating a contrast between Q_u and Q_d, a sign of the presence of (multiple) UGRs. By inputting the parameters corresponding to these UGRs into a COMSOL eigensolver, we indeed find typical UGR field profiles as shown in Fig. 4 (detailed later on). By inspecting Figs. 3(b) and 3(c), one observes that two families of UGRs arise.

The first family, indicated by a red dashed line and the red circle, arises from the interaction of the two Bloch modes near an anticrossing point. This family is analogous to what was previously observed [31] and originates from an accidental BIC in the same regions [red circle on Fig. 3(a) for symmetric structure]. Figure 4(a) (for a BIC), 4(b), and 4(c) (for UGRs) show the out-of-plane electric field profiles of these resonances. It is readily observed that these modes have similar profiles. By breaking the top-down symmetry (by creating the step), the reflection conditions at the upper side of the structure are slightly altered, allowing resonances at slightly different locations in parameter space and, consequently, the emergence of two nearby UGRs emitting in opposite directions. [The separation between the two UGRs is more visible on Figs. 5(d)–5(f), with blue and red zones next to each other, e.g., in the region around $\omega = 0.36(2\pi c/a)$ and $L_d/a = 0.5$.]

The second family [blue dashed line and circle in Figs. 3(b) and 3(c)] is uncommon and seems to emerge as an echo of a symmetry-protected BIC. The dominant mode for this BIC is horizontally antisymmetric and cannot couple with external radiation at the gamma point ($k_x = 0$). By imposing a nonzero k_x, the mode is allowed to couple to the outside, as shown by the profile in Fig. 4(d), transitioning from a true BIC to a qBIC emitting weak radiation outward. Adding broken up-down symmetry (the step) modifies the way the different guided modes interact, allowing for the occurrence of accidental destructive interference in a single direction, and thus the emergence of a UGR, visible in Fig. 4(e). This hypothesis is further confirmed by Figs. 5(d)–5(f) [e.g., around $\omega = 0.35(2\pi c/a)$ and $L_d/a = 1$], indicating the emergence of stronger UGRs from this family as the step asymmetry increases. This interaction happens at crossings that in the symmetric case do not interact [vertically orthogonal Fabry–Pérot modes, blue circle in Fig. 3(a)], but which can couple slightly when there is a step [so the Fabry–Pérot profiles are not fully orthogonal any longer, blue circle in Fig. 3(c)].

To summarize, both families of modes are connected with true (symmetry-protected) BICs in the symmetric structure at $k_x = 0$. The first family of pairs of UGRs is a consequence of a remaining (slightly) multimodal BIC in the symmetric structure at $k_x = 0.193(2\pi/a)$ [red circle, Fig. 3(a)]. In contrast, the second family of single UGRs originates from a true BIC in the symmetric structure (at $k_x = 0$) that disappears for a nonzero k_x [blue circle, Fig. 3(a)].

By gradually varying the parameter k_x, the resonance position shifts in the parameter space. This characteristic is related to the topological nature of BICs, providing them with a certain robustness against changes [7]. Introducing a symmetry breaking allows the BIC to split into multiple UGRs, which in turn move within the parameter space, as already observed in Refs. [22,37].

Figure 4(f) shows the ratio Q_d/Q_u for the first two resonance branches. This parameter can be interpreted as an asymmetry parameter for the radiation. The red and blue points represent the results obtained using an eigensolver (COMSOL), while the yellow and purple points correspond to results obtained using the multimodal method. The good agreement between the two methods demonstrates the effectiveness of the multimodal decomposition. Points e), b), and c) correspond to the asymmetry peaks associated with the profiles shown in Figs. 4(b), 4(c), and 4(e).

By analyzing a cross section in the upper and lower parts, it is possible to obtain a complete detail of the mode distribution in the staircase. We examine the UGR of Fig. 4(e). In the lower

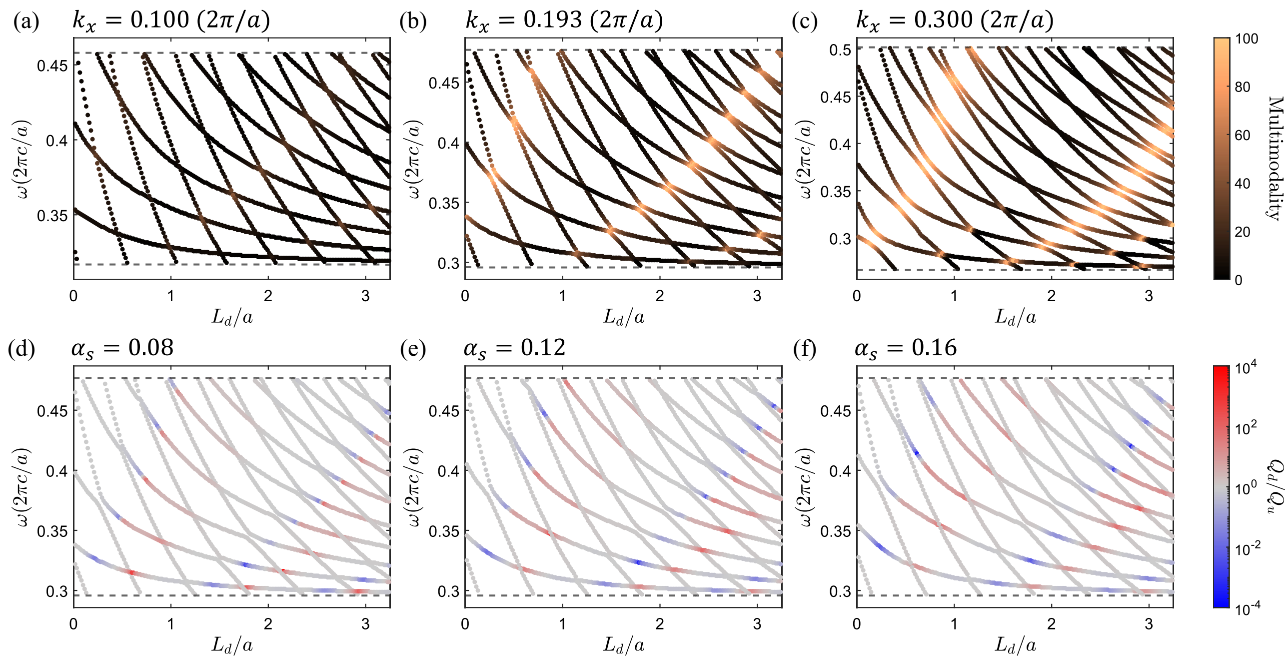

Fig. 5. (a)–(c) Sweep for $k_x = 0.100, 0.193$, and $0.300(2\pi/a)$, respectively, $\alpha_s = 0.08$. The color scale represents multimodality from 0 to 100%. A value of 0% indicates single-mode domination, while 100% indicates a 50/50 mixture. (d)–(f) Sweep for $\alpha_s = 0.08$, 0.12, and 0.16, respectively, $k_x = 0.193(2\pi/a)$. The color indicates the ratio Q_d/Q_u, with red indicating an UGR emitting upward and blue indicating an UGR emitting downward.

part, the mixing is relatively monomodal, consisting of approximately 93% of mode 2 and 7% of mode 1 in both upward propagation and downward propagation. In the upper part, the mixing is more asymmetric. Specifically, in the upward propagation, the mixing is 81% and 19%, while in the downward direction, it is 95% and 5%, respectively. This is explained by a surprisingly high reflectivity of mode 2 at the interface formed by the step. Figure 2(b) shows that more field is located near the edge of the waveguide for mode 2, making it more sensitive to the step. Despite a very small perturbation, 20% of mode 2 is reflected at the step interface.

This asymmetric behavior in the upper and lower parts of the structure indicates the formation mechanism of the UGR. By combining the mixing information with the interface reflectivity values (R_u and R_d), it turns out that the energy escaping on the side without emission is very similar for each mode independently, which enables destructive interference between the radiations of each mode when they couple. On the side with emission, the energy loss levels for each mode differ, preventing complete destructive interference.

For further exploration, we also perform sweeps for the interesting parameters k_x and α_s; see Fig. 5. From Figs. 5(a)–5(c), we vary the lateral Bloch propagation constant k_x, where the color indicates "multimodality." A value of 0% corresponds to a resonance dominated by a single guided mode. A value of 100% corresponds to a perfectly balanced mixture between the two modes, so 50% of the power in mode 1 and 50% in mode 2. We observe that increasing k_x enhances the coupling between the modes, thereby increasing the multimodal nature of the resonances. For the first family of UGRs, the anticrossing increases strongly, and the modes become multimodal over a larger parameter range (larger, brighter spot). The second family of UGRs also brightens, so becomes more mixed, as k_x increases, even though it is still fairly dominated by a single mode.

Figures 5(d)–5(f) show the ratio between Q_d and Q_u in function of α_s. A positive ratio exponent indicates an upward-radiating UGR (in red), while a negative ratio exponent indicates a downward-radiating UGR (in blue). It is clear that the UGRs we have seen before in Figs. 3(b) and 3(c) [with the same parameters as Figs. 5(b) and 5(d)] shift as α_s increases, indicating a significant influence of asymmetry on their position. The double UGRs from the first family are nicely visible in this figure: close to the anticrossing, pairs of red and blue zones can be observed, indicating the presence of a pair of UGRs radiating in opposite directions. In opposition, near the crossing, a single red dot is visible, meaning the apparition of only one UGR.

The application of the model to this 2D geometry demonstrates that it allows for analysis and understanding of multiple parameters on the UGRs, thereby facilitating the design of structures that support these types of resonances. In the next section, we explore a fully 3D example.

4. APPLICATION TO A 3D STRUCTURE

One of the strengths of the model is its versatility. In the previous section, we applied it to a 2D structure supporting two guided modes. In this section, we apply the model to a 2D array of finite 3D cylindrical pillars, where we break both size and position symmetries of the lattice [38]. This structure closely resembles the one used in Ref. [33] for sensing experiments. In Ref. [33], a good agreement between the experimental results and scattering simulations was reported, using plane-wave incidence to extract an extinction spectrum and identify resonances. Here,

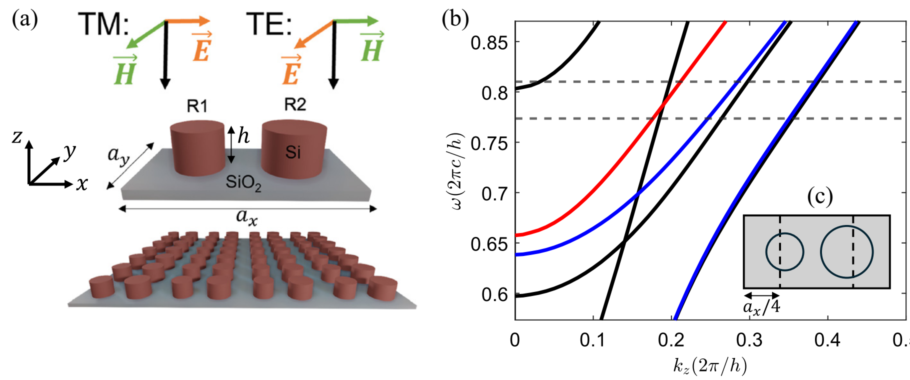

Fig. 6. (a) 3D representation of the structure. (b) Dispersion of the guided Bloch modes in the z direction. The horizontal dashed lines indicate the positions of the two studied TE-excited qBICs. The red curve (fifth line from the left) represents the main mode forming the low-λ qBIC. The blue lines (second and fourth lines from the left) correspond to the two modes forming the high-λ qBIC. (c) Cut of the structure showing the small offset of the cylinders.

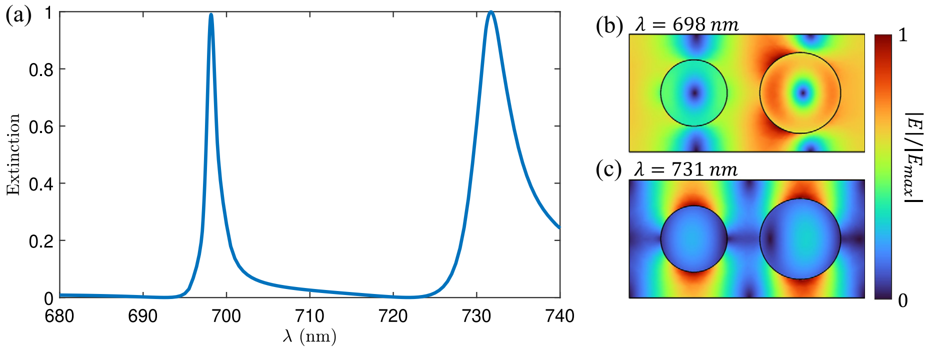

Fig. 7. (a) Extinction at normal incidence versus wavelength via a scattering simulation. Scattering electric field norm profile for (b) low-λ qBIC and (c) high-λ qBIC.

we apply the multimodal method in order to understand the qBICs in this device from another perspective and to work with an experimentally feasible structure.

Each unit cell, see Fig. 6(a), has a length of $a_x = 408$ nm and a width of $a_y = 204$ nm. The surrounding is considered uniform with a refractive index $n = 1.48$ (which was created with index-matching liquid in Ref. [33]), and the two cylinders per unit cell have index $n = 4.4$. Here, we restrict ourselves to nondispersive materials with a refractive index similar to those in Ref. [33], so that the (Bloch) mode dispersion is purely due to the geometry. The cylinders have a height of $h = 90$ nm and radii of $R_1 = 57.5$ nm and $R_2 = 70$ nm, respectively. Both cylinders are slightly offset from a square grid by 10 nm on the x axis; see Fig. 6(c).

The double breaking of symmetry (in both size and position of the cylinders) enables the emergence of multiple qBICs. Note that only breaking the position symmetry typically does not lead to qBICS, as inversion symmetry is conserved [38]. With our model, the resonances are found in a frequency range that permits up to seven guided modes of the transverse section, as shown in Fig. 6(b), which shows the modes (with all polarizations) as if the cylinders are infinitely long in the z direction and $k_x = k_y = 0$. In contrast to the previous 2D section [with Bloch modes of a 1D profile $n(x)$], here we cut the 3D cylinders in the middle, leading to a 2D refractive index profile $n(x, y)$ [see Fig. 6(c)]. The dispersion of the modes of this 2D PhC crystal array, considered infinite along the z direction, is depicted in Fig. 6(b). Although the multimodal method allows for all polarizations, we limit ourselves here to TE-excited qBICs, for which the field is primarily oriented along y as shown in Fig. 6(a).

Figure 7(a) shows the extinction spectrum via COMSOL scattering simulations of the structure, with TE excitation at normal incidence. Two qBICs appear in the spectrum, with extinction values approaching 1. Figures 7(b) and 7(c) display the electric field profile on a cut at mid-height of the cylinders for the two qBICs located at 698 nm (called "low-λ qBIC") and 731 nm ("high-λ qBIC"), respectively.

By applying our model to this structure, we can see that the nature of the two qBICs is different, e.g., via their decomposition. The low-λ qBIC is mainly composed of a single magnetic-dipole-type mode. The exact decomposition is 94% of the primary mode indicated in red in Fig. 6(b), 5% of a secondary mode, and less than 1% of other modes. The profile of the primary mode is visible in Fig. 8(a), showing a circulation of the electric field in the cylinders, akin to a magnetic dipole. This characterizes this resonance as a Fabry–Pérot-like qBIC.

To use the multimodal analysis, we divide the structure in two halves, needed to compute the scattering–reflection matrices, S_u and S_d. Then one alternative way to obtain a field profile of a mode is to inject the correct distribution of Bloch modes [of the section $n(x, y)$] in one half of the structure. In this way, by injecting directly the corresponding modes with their

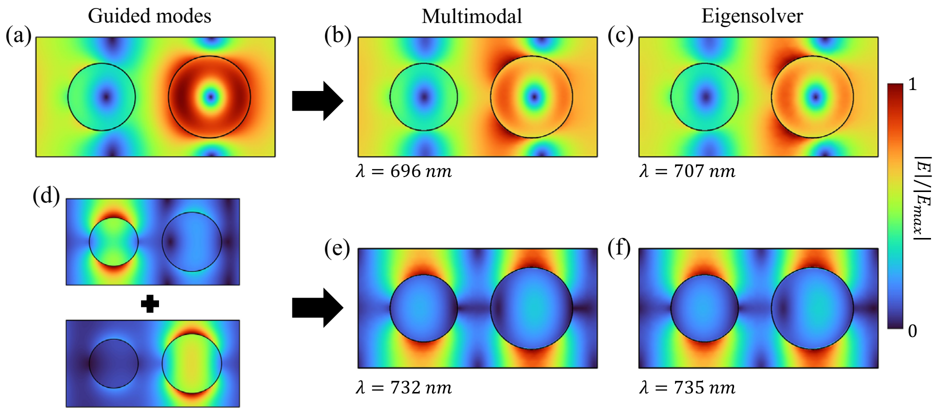

Fig. 8. (a)–(c) Electric field norm profiles for the low-λ qBIC. (d)–(f) electric field norm profiles for the high-λ BIC. (a) and (d) show guided modes in the cylinder section. (b) and (e) show fields at mid-height of the cylinders using the multimodal method. (c) and (f) show the profiles of the same modes obtained using an eigensolver.

eigenvector amplitudes into the top half of the structure, we get the profile of Fig. 8(b), plotted at the mid-height position of the cylindrical pillars. The correspondence with the profiles obtained in two other ways, i.e., by the scattering [Fig. 7(b)] and by the eigensolver [using the complete structure, Fig. 8(c)], is clear.

On the other hand, the high-λ qBIC consists of two modes represented in blue in Fig. 6(b) with a composition of 79% of the first mode and 21% of the second. Their profiles are shown in Fig. 8(d), representing electric-dipolar-type modes localized mainly in one of the cylinders. The presence in reasonable quantity of at least two modes characterizes this resonance as a Friedrich–Wintgen-type qBIC. Similar to the low-λ qBIC, the profiles obtained by different methods correspond almost perfectly with one another [see Figs. 7(c), 8(e), and 8(f)].

For both qBICs, one observes slightly more field inside the cylinders via the guided modes [Fig. 8(a)] than in the other types of profiles because the guided mode profiles are for an infinite waveguide, whereas the other profiles are at the middle of the finite cylinders (with interfering modes propagating back and forth). It is also worth noting that we obtain a good match for the wavelengths via the different methods (multimodal, scattering, and eigensolver), with a difference of approximately 3 nm for the low-λ qBIC and about 15 nm for the high-λ qBIC.

An interesting aspect is the relatively large wavelength of these qBICs, which is more than seven times larger than the height (90 nm) of the structure. For a basic fundamental Fabry–Pérot mode, one would think of the wavelength (in the material, or effective) divided by 2. Here, the relatively short length for the fundamental mode is due to the phase shift of the mode reflections and the stretching of the resonance into the layers above and below. Indeed, for a single-mode Fabry–Pérot, one needs

$$2\beta h + 2\varphi = 2\pi m, \tag{9}$$

where β is the propagation constant, φ is the reflection phase, and m is an integer. The phase of the reflection in our model is directly captured by the matrices R_u and R_d, nicely describing the "thinness" of the modes.

In the end, the decomposition method offers a different way to understand the resonances in this structure. In Ref. [33], different sensitivities to parameter modifications of the two qBICs were reported, offering sensor possibilities. We describe in Ref. [33] these behaviors via the percentage of energy located inside versus outside of the cylindrical pillars. Here, we show that the two qBICs have a different origin, with one being weakly multimodal and the other highly multimodal. The nearly monomodal qBIC stems from a magnetic-dipole guided mode, with the electric field fairly outside the cylinders. In contrast, the bimodal qBIC derives from two electric-dipole guided modes, with a more confined field. This type of reasoning thus provides an additional pathway to understand these and other types of behaviors.

5. CONCLUSION

We present a multimodal model that focuses on Bloch modes propagating in the out-of-plane direction of a PhC. We demonstrate that it is possible to describe BIC and UGR resonances as interactions between several modes reflecting back-and-forth in the PhC. The coupling of these modes via the interfaces enables destructive interference that can prevent radiation losses, either from both sides of the PhC, for BICs, or from only one side, for UGRs. The ability to quickly scan parts of a parameter space forms a significant advantage in locating and designing the resonances.

By applying the model to a 1D periodic structure with up-down symmetry breaking, we show that the model identifies asymmetric resonances, thereby enabling the rapid identification of UGRs oriented both upward and downward. Furthermore, the detailed guided mode decomposition allows one to understand in greater detail the mechanism behind these resonances and the impact of various parameters. Additionally, we demonstrate the model for a complex 3D structure, which permits the coexistence of numerous modes, thus helping to understand the nature of qBICs that were experimentally observed in Ref. [33].

In the end, the versatility of this model allows application to a wide range of structures, leading to a different way to classify and understand the resonances. It is therefore entirely feasible to apply this method to structures hosting specific effects, such as slot waveguides or second harmonic generation, in order to enhance control over applications of BICs in lasers and integrated devices.

Acknowledgment. The authors would like to thank Tom Van Loon, Minpeng Liang, and Jaime Gómez Rivas for inspiring us to test our model on a 3D structure and to compare our results with experimental data. We also appreciate their insightful feedback during the writing of this paper.

Disclosures. The authors declare no conflicts of interest.

Data availability. Data underlying the results presented in this paper are not publicly available at this time but may be obtained from the authors upon reasonable request.

REFERENCES

1. J. D. Joannopoulos, P. R. Villeneuve, and S. Fan, "Photonic crystals: putting a new twist on light," Nature **386**, 143–149 (1997).
2. S. Fan and J. D. Joannopoulos, "Analysis of guided resonances in photonic crystal slabs," Phys. Rev. B **65**, 235112 (2002).
3. C. W. Hsu, B. Zhen, J. Lee, *et al.*, "Observation of trapped light within the radiation continuum," Nature **499**, 188–191 (2013).
4. C. W. Hsu, B. Zhen, A. D. Stone, *et al.*, "Bound states in the continuum," Nat. Rev. Mater. **1**, 16048 (2016).
5. Y. Plotnik, O. Peleg, F. Dreisow, *et al.*, "Experimental observation of optical bound states in the continuum," Phys. Rev. Lett. **107**, 183901 (2011).
6. K. Koshelev, G. Favraud, A. Bogdanov, *et al.*, "Nonradiating photonics with resonant dielectric nanostructures," Nanophotonics **8**, 725–745 (2019).
7. B. Zhen, C. W. Hsu, L. Lu, *et al.*, "Topological nature of optical bound states in the continuum," Phys. Rev. Lett. **113**, 257401 (2014).
8. G. Roelkens, D. Van Thourhout, and R. Baets, "High efficiency silicon-on-insulator grating coupler based on a poly-silicon overlay," Opt. Express **14**, 11622–11630 (2006).
9. S. I. Azzam and A. V. Kildishev, "Photonic bound states in the continuum: from basics to applications," Adv. Opt. Mater. **9**, 2001469 (2020).
10. M. V. Gorkunov, A. A. Antonov, and Y. S. Kivshar, "Metasurfaces with maximum chirality empowered by bound states in the continuum," Phys. Rev. Lett. **125**, 093903 (2020).
11. S. Joseph, S. Pandey, S. Sarkar, *et al.*, "Bound states in the continuum in resonant nanostructures: an overview of engineered materials for tailored applications," Nanophotonics **10**, 4175–4207 (2021).
12. A. Overvig, N. Yu, and A. Alù, "Chiral quasi-bound states in the continuum," Phys. Rev. Lett. **126**, 073001 (2021).
13. L. Kühner, F. J. Wendisch, A. A. Antonov, *et al.*, "Unlocking the out-of-plane dimension for photonic bound states in the continuum to achieve maximum optical chirality," Light Sci. Appl. **12**, 250 (2023).
14. L. Huang, S. Li, C. Zhou, *et al.*, "Realizing ultrahigh-Q resonances through harnessing symmetry-protected bound states in the continuum," Adv. Funct. Mater. **34**, 2309982 (2023).
15. M. V. Gorkunov, A. A. Antonov, A. V. Mamonova, *et al.*, "Substrate-induced maximum optical chirality of planar dielectric structures," Adv. Opt. Mater. **13**, 2402133 (2024).
16. N. D. Le, P. Bouteyre, A. Kheir-Aldine, *et al.*, "Super bound states in the continuum on a photonic flatband: concept, experimental realization, and optical trapping demonstration," Phys. Rev. Lett. **132**, 173802 (2024).
17. J. Wang, J. Kühne, T. Karamanos, *et al.*, "All-dielectric crescent metasurface sensor driven by bound states in the continuum," Adv. Funct. Mater. **31**, 2104652 (2021).
18. T. Weber, L. Kühner, L. Sortino, *et al.*, "Intrinsic strong light-matter coupling with self-hybridized bound states in the continuum in van der Waals metasurfaces," Nat. Mater. **22**, 970–976 (2023).
19. C. Zhou, L. Huang, R. Jin, *et al.*, "Bound states in the continuum in asymmetric dielectric metasurfaces," Laser Photonics Rev. **17**, 2200564 (2022).
20. K. Koshelev, S. Kruk, E. Melik-Gaykazyan, *et al.*, "Subwavelength dielectric resonators for nonlinear nanophotonics," Science **367**, 288–292 (2020).
21. S. You, H. He, Y. Zhang, *et al.*, "Resonance wavelength stabilization of quasi-bound states in the continuum constructed by symmetry breaking and area compensation," Nano Lett. **24**, 15300–15307 (2024).
22. X. Yin, J. Jin, M. Soljačić, *et al.*, "Observation of topologically enabled unidirectional guided resonances," Nature **580**, 467–471 (2020).
23. X. Yin, T. Inoue, C. Peng, *et al.*, "Topological unidirectional guided resonances emerged from interband coupling," Phys. Rev. Lett. **130**, 056401 (2023).
24. B. Wang, J. Jiang, and G. P. Nordin, "Compact slanted grating couplers," Opt. Express **12**, 3313–3326 (2004).
25. A. Michaels and E. Yablonovitch, "Inverse design of near unity efficiency perfectly vertical grating couplers," Opt. Express **26**, 4766–4779 (2018).
26. Z. Li, X.-W. Luo, and Q. Gu, "Topological on-chip lasers," APL Photonics **8**, 070901 (2023).
27. W. Liu, W. Liu, L. Shi, *et al.*, "Topological polarization singularities in metaphotonics," Nanophotonics **10**, 1469–1486 (2021).
28. H. M. Doeleman, F. Monticone, W. den Hollander, *et al.*, "Experimental observation of a polarization vortex at an optical bound state in the continuum," Nat. Photonics **12**, 397–401 (2018).
29. M. Gong, J. Liu, L. Ge, *et al.*, "Multipolar perspective on unidirectional guided resonances," Phys. Rev. A **108**, 013522 (2023).
30. M. Hammer, "Resonant coupling of dielectric optical waveguides via rectangular microcavities: the coupled guided mode perspective," Opt. Commun. **214**, 155–170 (2002).
31. B. Maes, M. Ibanescu, J. D. Joannopoulos, *et al.*, "Microcavities based on multimodal interference," Opt. Express **15**, 6268–6278 (2007).
32. A. I. Ovcharenko, C. Blanchard, J.-P. Hugonin, *et al.*, "Bound states in the continuum in symmetric and asymmetric photonic crystal slabs," Phys. Rev. B **101**, 155303 (2020).
33. T. van Loon, M. Liang, T. Delplace, *et al.*, "Refractive index sensing using quasi-bound states in the continuum in silicon metasurfaces," Opt. Express **32**, 14289–14299 (2024).
34. H. A. Haus, *Waves and Fields in Optoelectronics*, Prentice-Hall Series in Solid State Physical Electronics (Prentice Hall, 1983).
35. P. Lalanne, C. Sauvan, and J. Hugonin, "Photonics confinement in photonic crystal nanocavities," Laser Photonics Rev. **2**, 514–526 (2008).
36. K. Koshelev, S. Lepeshov, M. Liu, *et al.*, "Asymmetric metasurfaces with high-Q resonances governed by bound states in the continuum," Phys. Rev. Lett. **121**, 193903 (2018).
37. S. Mukherjee, J. Gomis-Bresco, D. Artigas, *et al.*, "Unidirectional guided resonances in anisotropic waveguides," Opt. Lett. **46**, 2545–2548 (2021).
38. S. Murai, D. R. Abujetas, L. Liu, *et al.*, "Engineering bound states in the continuum at telecom wavelengths with non-Bravais lattices," Laser Photonics Rev. **16**, 2100661 (2022).